nature physics

LETTERS

https://doi.org/10.1038/s41567-021-01171-w

Check for updates

Correlated insulating states at fractional fillings of the WS_2/WSe_2 moiré lattice

Xiong Huang[1,2,9], Tianmeng Wang[3,9], Shengnan Miao[3,9], Chong Wang[4,9], Zhipeng Li[3], Zhen Lian[3], Takashi Taniguchi[5], Kenji Watanabe[6], Satoshi Okamoto[7], Di Xiao[4]✉, Su-Fei Shi[3,8]✉ and Yong-Tao Cui[1]✉

The strong electron interactions in the minibands formed in moiré superlattices of van der Waals materials, such as twisted graphene and transition metal dichalcogenides, make such systems a fascinating platform with which to study strongly correlated states[1–19]. In most systems, the correlated states appear when the moiré lattice is filled by an integer number of electrons per moiré unit cell. Recently, correlated states at fractional fillings of 1/3 and 2/3 holes per moiré unit cell have been reported in the WS_2/WSe_2 hetero-bilayer, hinting at the long-range nature of the electron interaction[16]. Here we observe a series of correlated insulating states at fractional fillings of the moiré minibands on both electron- and hole-doped sides in angle-aligned WS_2/WSe_2 hetero-bilayers, with certain states persisting at temperatures up to 120 K. Simulations reveal that these insulating states correspond to ordering of electrons in the moiré lattice with a periodicity much larger than the moiré unit cell, indicating a surprisingly strong and long-range interaction beyond the nearest neighbours.

Band theory predicts that a partially filled energy band should produce a metallic state. However, when the electron interaction becomes considerable, insulating states can appear at partial fillings of the band. A well-known example is the Mott insulator state at half filling, in which strong on-site Coulomb repulsion prevents double occupancy on the same lattice site, resulting in electron localization with exactly one electron per lattice site[20,21]. If we go beyond on-site repulsion, inter-site interactions can lead to even more exotic correlated states at other fractional band fillings, corresponding to commensurate occupation of the lattice sites, such as fractional Chern insulators[22], charge density waves[23], checkerboard and stripe phases[24,25] and Wigner crystals[26–30]. Recently, moiré superlattices based on van der Waals heterostructures of two-dimensional (2D) materials have emerged as a new playground for engineering correlated states[1–19]. The formation of a periodic moiré structure with lattice size on the mesoscopic length scale (on the order of tens of nanometres) results in flat minibands with much reduced kinetic energies, while the Coulomb interaction is strongly enhanced due to the reduced screening in two dimensions. Correlated states, including Mott insulators and superconductivity, have been observed in various versions of twisted graphene layers at small angles[1–14]. The Mott insulator states appear at fillings of the minibands corresponding to one, two and three electrons per moiré unit cell. Very recently, it has been shown that the electron interaction is even further strengthened in angle-aligned hetero-bilayers of transition metal dichalcogenides (TMDs)[15–19,31,32], including WS_2/WSe_2 (refs. [16,17,31,32]), WSe_2/WSe_2 (ref. [19]) and WSe_2/hBN/WSe_2 (ref. [18]) systems (where hBN is hexagonal boron nitride). The Mott insulator state at the filling of one hole per moiré unit cell[16,17,19] and generalized Wigner crystal states at fillings of 1/3 and 2/3 holes per moiré unit cell[16] have been reported, indicating strong interactions on site and among nearest neighbours (NNs), but these correlated states have only been observed on the hole-doped side. It is intriguing to explore whether these correlated states would form on the electron-doped side and, more importantly, whether the strong interaction can extend beyond NNs to induce correlated states at more complex commensurate fillings of the underlying moiré lattice.

In this Letter, we report the observation of a series of correlated insulating states for both electron- and hole-doped regimes in a WS_2/WSe_2 moiré heterostructure, including states at fillings of $n=\pm1$ (one electron (+1) or hole (−1) per moiré unit cell) and, more excitingly, correlated insulating states at a series of fractional fillings including $n=+1/6, \pm1/4, \pm1/3, \pm1/2, \pm2/3, \pm3/4, +5/6$ and $\pm3/2$. Monte Carlo (MC) simulations of a Coulomb gas model suggest that they correspond to long-range orderings of electrons in the moiré lattice with spatial patterns of various triangular and stripe phases. In one sample, we find that the transition temperature for $n=\pm1/3$ and $\pm2/3$ can be as high as 120 K, and additional fillings at $n=-8/9, -5/6, -7/9, +5/9$ and $+6/7$ are also observed, indicating that an unexpectedly strong interaction is achieved in this sample.

The typical structure of our devices is shown in Fig. 1a. Angle-aligned monolayers of WS_2 and WSe_2 are encapsulated by hBN flakes, and thin graphite flakes are used as both the electrical contact and bottom gate electrodes (see Methods and Extended Data Fig. 1 for more details of device fabrication and characterization). The lattice constants of WS_2 and WSe_2 have a 4% mismatch, which creates a moiré pattern with a periodicity of ~8 nm when the two monolayers are aligned precisely at either 0° or 60°. Multiple minibands should form on both the electron- and hole-doped sides, with the conduction band minimum and valence band maximum locating in different layers according to the type-II band alignment

[1]Department of Physics and Astronomy, University of California, Riverside, CA, USA. [2]Department of Materials Science and Engineering, University of California, Riverside, CA, USA. [3]Department of Chemical and Biological Engineering, Rensselaer Polytechnic Institute, Troy, NY, USA. [4]Department of Physics, Carnegie Mellon University, Pittsburgh, PA, USA. [5]International Center for Materials Nanoarchitectonics, National Institute for Materials Science, Tsukuba, Japan. [6]Research Center for Functional Materials, National Institute for Materials Science, Tsukuba, Japan. [7]Materials Science and Technology Division, Oak Ridge National Laboratory, Oak Ridge, TN, USA. [8]Department of Electrical, Computer and Systems Engineering, Rensselaer Polytechnic Institute, Troy, NY, USA. [9]These authors contributed equally: Xiong Huang, Tianmeng Wang, Shengnan Miao, Chong Wang. ✉e-mail: dixiao@cmu.edu; shis2@rpi.edu; yongtao.cui@ucr.edu

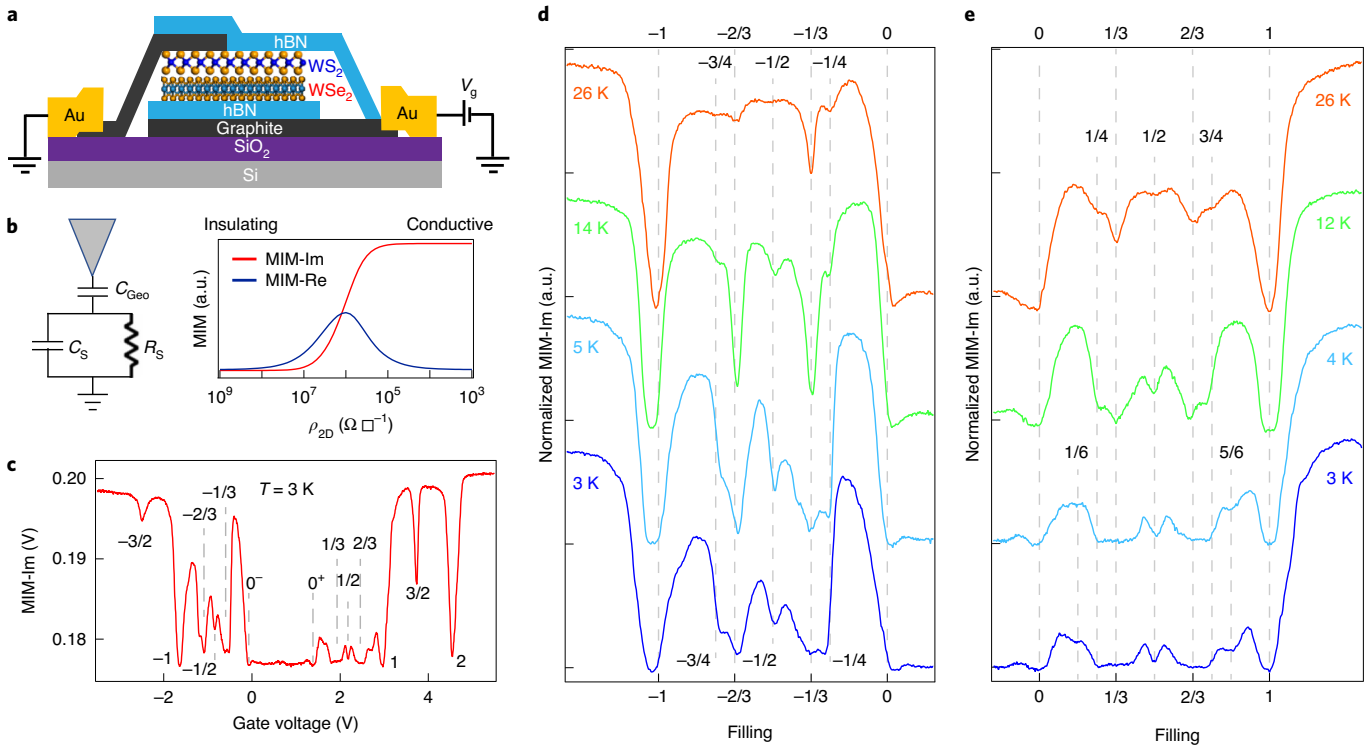

Fig. 1 | Spectrum of the correlated insulating states in device D1. a, Schematic of the device structure. V_g is the gate voltage. **b**, Effective circuit model for the tip–sample impedance probed by MIM, and a typical response curve showing MIM-Im and MIM-Re as a function of the 2D resistivity of the sample, ρ_{2D}. C_{Geo} denotes the geometric capacitance between the tip and sample, C_S and R_S denote the effective sample-to-ground capacitance and resistance, respectively, probed locally by the tip. **c**, MIM-Im versus gate voltage curve taken at $T = 3$ K. Dashed lines indicate the nominal positions of fractional fillings at $n = \pm 1/3$, $\pm 2/3$ and $\pm 1/2$, and the band edges at 0^+ and 0^-. **d**,**e**, MIM-Im versus calibrated filling at selected temperatures for the hole (**d**) and electron (**e**) doping sides.

in this hetero-bilayer[15,17,33,34]. Therefore, correlated insulating states can potentially appear on both electron- and hole-doped sides. To probe the insulating states we used scanning microwave impedance microscopy (MIM), which is capable of sensing the local resistivity of the sample (Fig. 1b)[35]. In MIM, a microwave signal in the frequency range of 1–10 GHz is routed to a sharp metal tip, and the reflected signal is analysed to extract the imaginary and real parts of the complex tip–sample impedance, which we call MIM-Im and MIM-Re, respectively (Methods)[36]. As the tip voltage oscillates, carriers in the sample move towards and away from the tip to screen the a.c. electric fields. Such screening capability is characterized by the MIM-Im signal. The MIM-Re signal, on the other hand, characterizes the dissipation generated by the oscillating current induced in the sample. Both channels depend on the sample resistivity, as shown in the typical MIM response curves in Fig. 1b. In general, MIM-Im decreases monotonically with increasing resistivity, and there is a finite sensitivity window outside which MIM signals become saturated.

Using MIM, we observe a series of insulating states at fractional filling levels in the WS_2/WSe_2 moiré lattice on both doping sides. We performed MIM measurements with the tip parked at a fixed spot over the sample while sweeping the gate voltage. Representative measurements taken at a temperature of $T = 3$ K are shown in Fig. 1c. At high doping levels on both electron and hole sides, the sample is highly conductive, resulting in a saturated high MIM-Im signal. As the doping is reduced from either side, the sample becomes more insulating and the MIM-Im signal decreases. In this process, a series of pronounced dips appear in the MIM-Im trace, indicating that the sample goes through several insulating states. The major dips exhibit a structure that is very similar for both electron and hole sides, corresponding to $n = \pm 1/3$, $\pm 1/2$, $\pm 2/3$, ± 1, $\pm 3/2$ and $+2$. (See Methods for details on the calibration of the filling values, Extended Data Fig. 2 regarding the $n = -2$ state and Extended Data Fig. 3 for spatial variations of the MIM spectrum.) There are also several fine features next to the major filling values mentioned above, but their features are not well separated from the major filling values, mostly because the sample resistivity is very high at $T = 3$ K and the MIM-Im signal becomes saturated at the lower limit. By raising the temperature slightly to reduce the resistivity, the fine features become more pronounced. Figure 1d,e presents traces of MIM-Im versus calibrated filling, n, at several temperatures from 3 K to 26 K. From these data, we identify the filling values for several additional states at $n = \pm 1/4$, $\pm 3/4$, $+1/6$ and $+5/6$. Among all the observed states, the $n = -1/3$, $-2/3$ and -1 states have been reported in recent works, in which the $n = -1$ state was interpreted as a Mott insulator[16,17] and the $n = -1/3$ and $-2/3$ states as generalized Wigner crystals[16]. According to the type-II band alignment in this system, the states at negative filling values correspond to filling of the valence miniband in the WSe_2 layer. Similarly, the ones at positive filling values correspond to filling of the conduction miniband in the WS_2 layer. In particular, the $n = +2$ state corresponds to the complete filling of the conduction miniband with two electrons per moiré unit cell.

For the $n = \pm 1$ Mott insulator states, the entire moiré lattice is uniformly occupied by exactly one electron or hole per moiré unit cell (Fig. 2a). For the generalized Wigner crystal states at $n = \pm 1/3$, one electron or hole fills in a set of three moiré unit cells so that charges can only occupy every second NN site, forming a triangular lattice as illustrated in Fig. 2b. The distance between neighbouring occupied sites is $\sqrt{3}a_0$, where a_0 is the distance between the NN

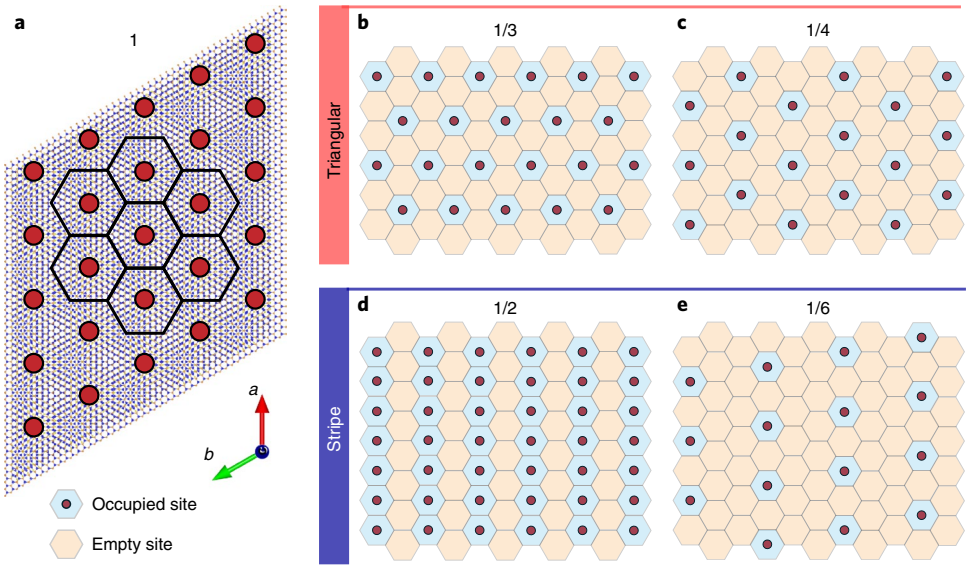

Fig. 2 | Ordering patterns at fractional fillings of the moiré lattice. a, Schematic of the triangular lattice for the WS_2/WSe_2 moiré superlattice, filled by one carrier per moiré unit cell. **b**,**c**, Patterns for the triangular lattice formed at fractional fillings of $n=1/3$ (**b**) and 1/4 (**c**). **d**,**e**, Patterns for the stripe phase formed at fractional fillings of $n=1/2$ (**d**) and 1/6 (**e**).

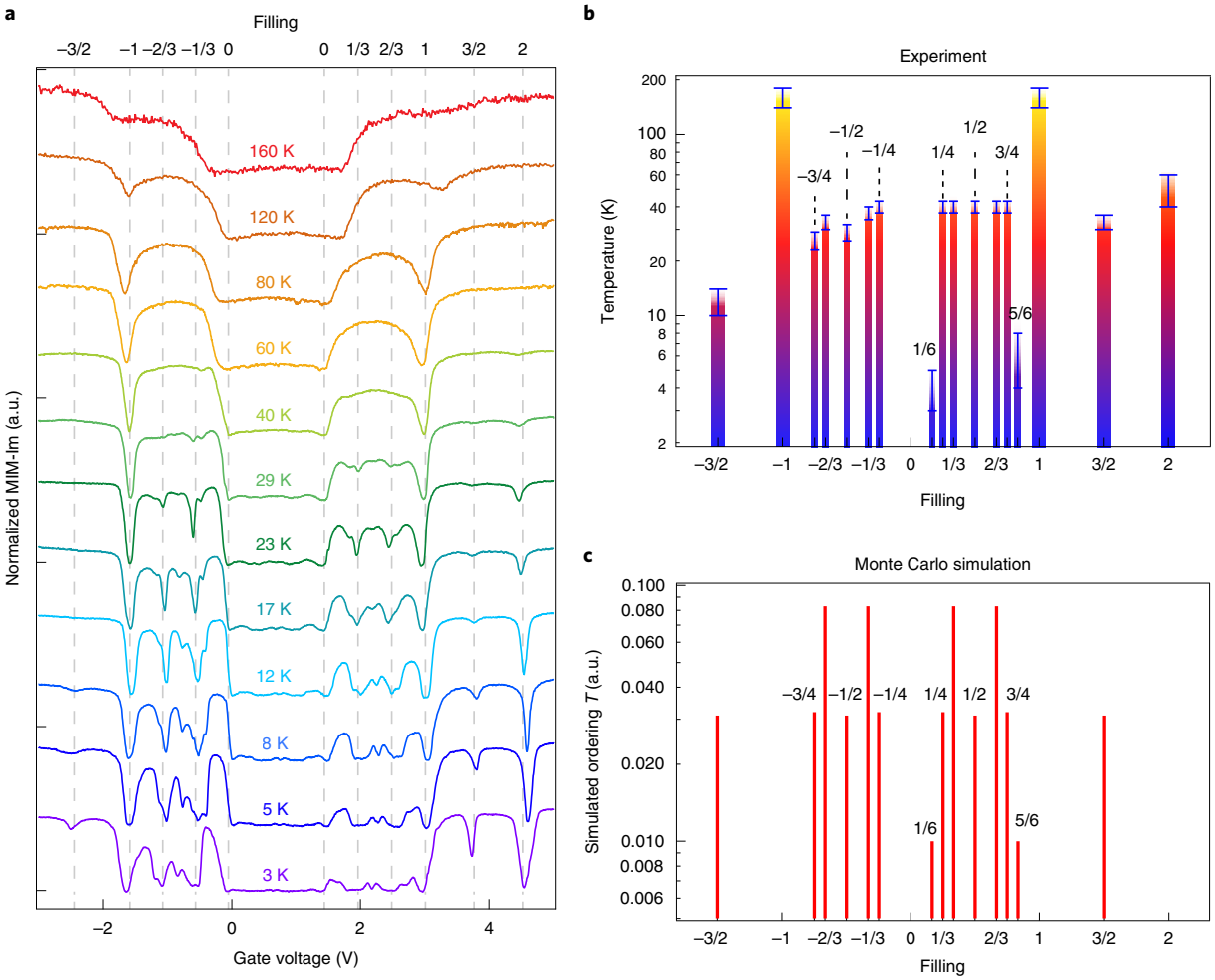

Fig. 3 | Temperature dependence of the correlated insulating states in device D1. a, MIM-Im versus gate voltage curves taken at temperatures from 3 K to 140 K. **b**, The temperature range in which the correlated insulating states can be resolved by MIM. **c**, The ordering temperatures obtained from MC simulations, for filling fractions corresponding to the experimentally observed values.

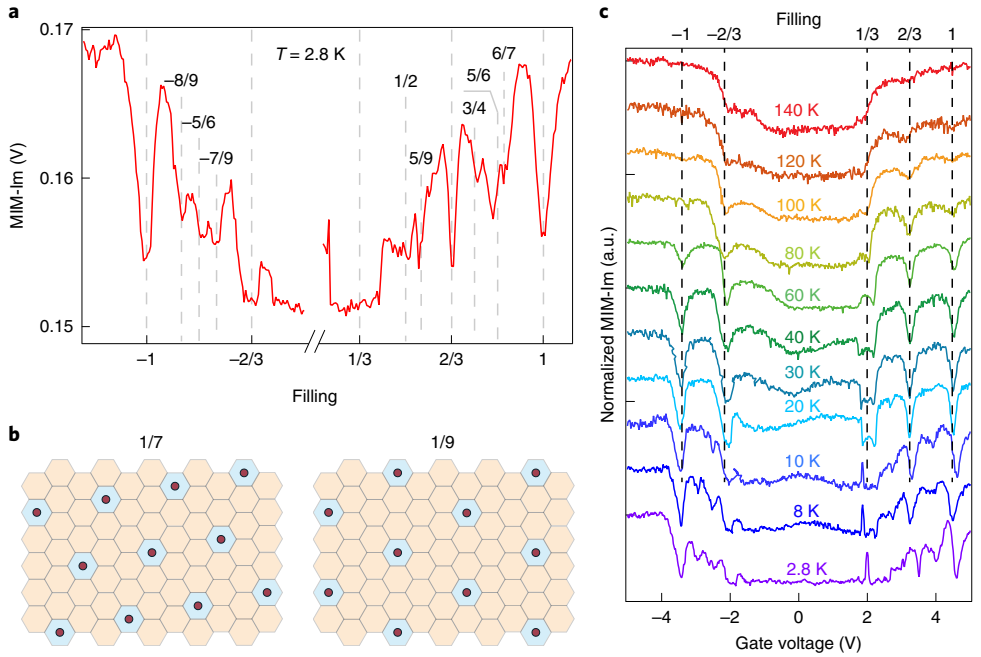

Fig. 4 | Correlated insulating states in device D2. a, MIM-Im versus calibrated filling at $T = 2.8$ K. Dashed lines indicate the nominal positions of fractional fillings (labelled). **b**, The spatial filling patterns for $n = 1/7$ and 1/9, obtained through MC simulation. **c**, Temperature dependence of the MIM-Im spectrum from 2.8 K to 140 K. Dashed lines indicated the positions for $n = +1/3$, $\pm 2/3$ and ± 1, determined from the high-temperature data.

sites in the moiré lattice. The $n = \pm 2/3$ states are simply complementary to $n = \pm 1/3$ by exchanging occupied and empty sites. All the other fractional fillings should correspond to more complex spatial patterns.

To gain more insights into the ordering patterns in these insulating states at fractional filling $|n| < 1$, we describe our system with a Coulomb gas model on a triangular lattice. For definiteness, we assume $n > 0$. The corresponding Hamiltonian reads

$$H = \frac{1}{2}\sum_{i,j} V_{ij}(n_i - n)(n_j - n)$$

where V_{ij} is the inter-site repulsion and $n_i = 0$ or 1 is the occupation number of site i. We have subtracted the average charge density, which is the filling fraction n, to ensure charge neutrality. This Hamiltonian is manifestly particle–hole symmetric; that is, the state at filling fraction $1 - n$ can be obtained from that at n by swapping occupied and empty sites. Here, we have neglected the kinetic energy completely. Because the period of the moiré lattice is relatively large ($a_0 \approx 8$ nm), long-range hopping should be exponentially suppressed. To capture the essence of the interaction effect, we consider the unscreened Coulomb interaction, $V_{ij} = 1/|\mathbf{R}_i - \mathbf{R}_j|$. Note that, in a 2D device with a nearby metallic gate, the Coulomb interaction is in general screened and can be approximated by $V(r) = 1/r - 1/\sqrt{r^2 + 4D^2}$, where D is the distance from the gate to the device. The unscreened Coulomb potential is therefore appropriate for large D.

We performed MC simulations based on this simple Coulomb gas model to search through filling fractions ranging from 0 to 1/2 (because filling fractions n and $1 - n$ are particle–hole symmetric) and identify the charge ordering patterns for the observed filling fractions (details on the simulation procedure are provided in the Methods), which can be grouped into two categories, triangular and stripe phases, as shown in Fig. 2. (More filling patterns for another device are presented later in Fig. 4.) The triangular phases include $n = 1/3$ and 1/4 (Fig. 2b,c). They match the observed filling values at $n = \pm 1/3$, $\pm 2/3$, $\pm 1/4$ and $\pm 3/4$. These states can be considered as generalized Wigner crystals[27], as a result of the competition between the long-range Coulomb interaction and the confining potential in the moiré lattice. They preserve the C_3 rotational symmetry of the original moiré lattice but break its translational symmetry (Extended Data Fig. 4 presents simulated patterns and domains for triangular lattices). In general, the triangular lattice can form for any filling value $n = 1/p$, where p is an integer such that $\sqrt{p}a_0$ matches the distance between two nearby neighbour sites. For example, the 1/3 state corresponds to the second NN separation, and the 1/4 state corresponds to the third NN.

On the other hand, the stripe phases further break the C_3 rotational symmetry and should occur for commensurate fractions at higher densities. We find that the stripe phase is a robust ground-state configuration for $n = 1/2$ and 1/6, corresponding to the $n = \pm 1/2$, +1/6 and +5/6 observed in our experiment. The $n = \pm 3/2$ states can be understood as adding carriers on top of uniformly occupied $n = \pm 1$ states, so they should be in the same stripe phase pattern as $n = 1/2$, if we ignore the specific occupation site within the moiré unit cell. Each stripe consists of a few rows, and a fraction of the sites are occupied according to the filling value. Neighbouring stripes have a translational shift along the stripe direction. The combination of intra-stripe occupation and inter-stripe shift minimizes the overall interaction energy of the system (Extended Data Fig. 5 presents simulated patterns and domains for the stripe phases). Transitions into the stripe phase at $n = 1/2$ and 1/6 have well-defined ordering temperatures, indicating their robustness against perturbations (Extended Data Fig. 6).

Next we study the temperature dependence of the insulating states to examine the melting of the charge ordering. Figure 3a presents MIM-Im versus gate voltage traces from 3 K to 160 K. The states at $n = \pm 1$ can be resolved at temperatures up to 120–160 K, which corresponds to energy gaps of 10–20 meV, consistent with recent studies[17]. The fractional fillings at $n = \pm 1/3$, $\pm 2/3$, $\pm 1/2$, $\pm 1/4$, $\pm 3/4$, +3/2 and +2 disappear at around 30–40 K. The $n = -3/2$ state disappears at around 10 K, while the $n = +1/6$ and +5/6 states disappear

at 4–6 K. Figure 3b plots the temperature ranges in which each filling can be resolved by MIM. The disappearance of the insulating states suggests that the carriers are no longer localized but can easily hop to nearby empty sites. We can then associate this characteristic temperature with the melting of the charge orders seen in the MC simulations at elevated temperatures (Extended Data Fig. 7). As a comparison, Fig. 3c presents the ordering temperatures obtained through our MC simulation (Extended Data Fig. 6), which match the experimental data well.

In device D2, we observe behaviours that indicate an even longer-range and stronger interaction than that in device D1. Figure 4a presents the MIM-Im spectrum as a function of calibrated filling measured at $T = 2.8$ K. Compared to device D1, we observe several new filling fractions, including $n = -8/9$, $-5/6$, $-7/9$, $+5/9$ and $+6/7$. Among these fillings, the $n = -5/6$ state is the counterpart to the $n = +5/6$ state observed in device D1, which has a stripe pattern. The $n = +6/7$ and $-8/9$ states are found to have triangular patterns by our MC simulation (plotted as 1/7 and 1/9, respectively, in Fig. 4b). The 1/7 filling corresponds to the fourth NN separation and the 1/9 corresponds to the fifth NN, much longer-range than the triangular lattice states observed in D1. The $n = +5/9$ and $-7/9$ states are two exceptions for which our simulations do not obtain well-defined transitions to the ground states (because of the many energetically close configurations; Extended Data Fig. 5). The $n = \pm 1/3$, $\pm 2/3$ and ± 1 states can be resolved at temperatures up to 100–120 K (Fig. 4c and Extended Data Fig. 8), while all other fractional fillings disappear at around 20–30 K. The transition temperature for $n = \pm 1/3$ and $\pm 2/3$ is much enhanced compared to our other samples as well as earlier studies[16], signalling a stronger interaction strength in device D2, which corroborates the observation of rich filling fractions. Although the mechanism for the interaction enhancement in D2 is not yet clear, we suspect that local strain or inhomogeneities could play a role (Extended Data Fig. 9 presents more data taken at nearby spots). Current-generation moiré devices are known to have large spatial inhomogeneities[37]. The spatial resolution of our MIM technique, on the order of 100 nm, allows us to detect local features that exhibit strong interactions. Further research is warranted to investigate how inhomogeneities could affect the correlated states locally.

Online content

Any methods, additional references, Nature Research reporting summaries, source data, extended data, supplementary information, acknowledgements, peer review information; details of author contributions and competing interests; and statements of data and code availability are available at https://doi.org/10.1038/s41567-021-01171-w.

Received: 21 July 2020; Accepted: 8 January 2021;
Published online: 15 February 2021

References

1. Bistritzer, R. & MacDonald, A. H. Moiré bands in twisted double-layer graphene. *Proc. Natl Acad. Sci. USA* **108**, 12233–12237 (2011).
2. Cao, Y. et al. Correlated insulator behaviour at half-filling in magic-angle graphene superlattices. *Nature* **556**, 80–84 (2018).
3. Cao, Y. et al. Unconventional superconductivity in magic-angle graphene superlattices. *Nature* **556**, 43–50 (2018).
4. Shen, C. et al. Correlated states in twisted double bilayer graphene. *Nat. Phys.* **16**, 520–525 (2020).
5. Cao, Y. et al. Tunable correlated states and spin-polarized phases in twisted bilayer–bilayer graphene. *Nature* **583**, 215–220 (2020).
6. Liu, X. et al. Tunable spin-polarized correlated states in twisted double bilayer graphene. *Nature* **583**, 221–225 (2020).
7. Chen, G. et al. Evidence of a gate-tunable Mott insulator in a trilayer graphene moiré superlattice. *Nat. Phys.* **15**, 237–241 (2019).
8. Chen, G. et al. Signatures of gate-tunable superconductivity in trilayer graphene/boron nitride moiré superlattice. *Nature* **572**, 215–219 (2019).
9. Sharpe, A. L. et al. Emergent ferromagnetism near three-quarters filling in twisted bilayer graphene. *Science* **365**, 605–608 (2019).
10. Serlin, M. et al. Intrinsic quantized anomalous Hall effect in a moiré heterostructure. *Science* **367**, 900–903 (2020).
11. Chen, G. et al. Tunable correlated Chern insulator and ferromagnetism in a moiré superlattice. *Nature* **579**, 56–61 (2020).
12. Chen, S. et al. Electrically tunable correlated and topological states in twisted monolayer–bilayer graphene. *Nat. Phys.* https://doi.org/10.1038/s41567-020-01062-6 (2020).
13. Polshyn, H. et al. Electrical switching of magnetic order in an orbital Chern insulator. *Nature* **588**, 66–70 (2020).
14. Shi, Y. et al. Tunable van Hove singularities and correlated states in twisted trilayer graphene. Preprint at https://arxiv.org/pdf/2004.12414.pdf (2020).
15. Wu, F., Lovorn, T., Tutuc, E. & MacDonald, A. H. H. Hubbard model physics in transition metal dichalcogenide moiré bands. *Phys. Rev. Lett.* **121**, 26402 (2018).
16. Regan, E. C. et al. Mott and generalized Wigner crystal states in WSe_2/WS_2 moiré superlattices. *Nature* **579**, 359–363 (2020).
17. Tang, Y. et al. Simulation of Hubbard model physics in WSe_2/WS_2 moiré superlattices. *Nature* **579**, 353–358 (2020).
18. Shimazaki, Y. et al. Strongly correlated electrons and hybrid excitons in a moiré heterostructure. *Nature* **580**, 472–477 (2020).
19. Wang, L. et al. Correlated electronic phases in twisted bilayer transition metal dichalcogenides. *Nat. Mater.* **19**, 861–866 (2020).
20. Mott, N. F. The basis of the electron theory of metals, with special reference to the transition metals. *Proc. Phys. Soc. A* **62**, 416–422 (1949).
21. Imada, M., Fujimori, A. & Tokura, Y. Metal–insulator transitions. *Rev. Mod. Phys.* **70**, 1039–1263 (1998).
22. Sheng, D. N., Gu, Z.-C., Sun, K. & Sheng, L. Fractional quantum Hall effect in the absence of Landau levels. *Nat. Commun.* **2**, 389 (2011).
23. Grüner, G. The dynamics of charge-density waves. *Rev. Mod. Phys.* **60**, 1129–1181 (1988).
24. Emery, V. J., Kivelson, S. A. & Tranquada, J. M. Stripe phases in high-temperature superconductors. *Proc. Natl Acad. Sci. USA* **96**, 8814–8817 (1999).
25. Hoffman, J. E. A four unit cell periodic pattern of quasi-particle states surrounding vortex cores in $Bi_2Sr_2CaCu_2O_{8+\delta}$. *Science* **295**, 466–469 (2002).
26. Wigner, E. On the interaction of electrons in metals. *Phys. Rev.* **46**, 1002–1011 (1934).
27. Hubbard, J. Generalized Wigner lattices in one dimension and some applications to tetracyanoquinodimethane (TCNQ) salts. *Phys. Rev. B* **17**, 494–505 (1978).
28. Grimes, C. C. & Adams, G. Evidence for a liquid-to-crystal phase transition in a classical, two-dimensional sheet of electrons. *Phys. Rev. Lett.* **42**, 795–798 (1979).
29. Andrei, E. Y. et al. Observation of a magnetically induced Wigner solid. *Phys. Rev. Lett.* **60**, 2765–2768 (1988).
30. Shapir, I. et al. Imaging the electronic Wigner crystal in one dimension. *Science* **364**, 870–875 (2019).
31. Xu, Y. et al. Correlated insulating states at fractional fillings of moiré superlattices. *Nature* **587**, 214–218 (2020).
32. Jin, C. et al. Stripe phases in WSe_2/WS_2 moiré superlattices. Preprint at https://arxiv.org/pdf/2007.12068.pdf (2020).
33. Jin, C. et al. Observation of moiré excitons in WSe_2/WS_2 heterostructure superlattices. *Nature* **567**, 76–80 (2019).
34. Zhang, Z. et al. Flat bands in twisted bilayer transition metal dichalcogenides. *Nat. Phys.* **16**, 1093–1096 (2020).
35. Lai, K., Kundhikanjana, W., Kelly, M. & Shen, Z. X. Modeling and characterization of a cantilever-based near-field scanning microwave impedance microscope. *Rev. Sci. Instrum.* **79**, 063703 (2008).
36. Cui, Y.-T., Ma, E. Y. & Shen, Z.-X. Quartz tuning fork based microwave impedance microscopy. *Rev. Sci. Instrum.* **87**, 063711 (2016).
37. Chu, Z. et al. Nanoscale conductivity imaging of correlated electronic states in WSe_2/WS_2 moiré superlattices. *Phys. Rev. Lett.* **125**, 186803 (2020).

Methods

Heterostructure device fabrication. We used a dry pick-up method[38] to fabricate the WS_2/WSe_2 heterostructures. The bulk crystals of WS_2 and WSe_2 were acquired from HQ Graphene, which were used for the exfoliation of monolayer WS_2 and monolayer WSe_2. For the aligned heterostructures we chose exfoliated monolayers with sharp edges, whose crystal axes were further confirmed by second harmonic generation (SHG) measurements. We then mounted the silicon substrate with a 285-nm thermal oxide layer on a rotational stage and clamped the glass slide with thin flakes to another 3D stage. The 3D stage could be adjusted to control the distance between the substrates and thin flakes, and we used an hBN flake to sequentially pick up the WSe_2 monolayer, WS_2 monolayer, the thin graphite contact and the second hBN flake onto the pre-patterned Au electrodes on Si substrates. We finely adjusted the angle of the rotational stage (accuracy of 0.02°) under a microscope objective to stack the monolayer WS_2 on the monolayer WSe_2, ensuring a near-zero twist angle between the two flakes. The final constructed device was annealed at 140 °C for 6 h in a vacuum chamber. The pre-patterned Au contact electrodes were fabricated using standard electron-beam lithography and electron-beam evaporation processes (Extended Data Fig. 1 presents optical microscope images of devices D1 and D2).

MIM measurements. The MIM measurements were performed on a home-built cryogenic scanning probe microscope platform. A small microwave excitation of ~0.1 μW at a fixed frequency around 10 GHz was delivered to a chemically etched tungsten tip mounted on a quartz tuning fork. The reflected signal was analysed to extract the demodulated output channels, MIM-Im and MIM-Re, which are proportional to the imaginary and real parts of the admittance between the tip and sample, respectively. To enhance the MIM signal quality, the tip on the tuning fork was excited to oscillate at a frequency of ~32 kHz with an amplitude of ~8 nm. The resulting oscillation amplitudes of MIM-Im and MIM-Re were then extracted using a lock-in amplifier to yield d(MIM-Im)/dz and d(MIM-Re)/dz, respectively. The d(MIM)/dz signals are free of fluctuating backgrounds, and their behaviour is very similar to that of standard MIM signals. In this Letter we simply refer to d(MIM)/dz as the MIM signal.

Determination of the alignment angle of the hetero-bilayer. The twist angle between WS_2 and WSe_2 flakes was measured by SHG (Extended Data Fig. 1). This was $1.1 \pm 0.3°$ off 60° alignment in device D1 and $2.2 \pm 0.3°$ off 0° alignment in device D2.

The angle can also be estimated from the charge density corresponding to the $n = 1$ state, n_0, calculated using a parallel capacitor model: $n_0 = \epsilon_0 \epsilon_r \Delta V_g / ed$, where ϵ_0 is the permittivity in vacuum, $\epsilon_r \approx 3-4$ is the dielectric constant of hBN, d is the thickness of the bottom hBN and e is the electron charge. The gate voltage ΔV_g is determined from the filling fraction calibration. For device D1, $d = 17.4$ nm and $\Delta V_g = 1.50$ V, we obtain $n_0 \approx 1.4 \times 10^{12}$ cm^{-2} to 1.9×10^{12} cm^{-2} corresponding to a twist angle that is <0.7° off 60° alignment. For device D2, $d = 23.3$ nm and $\Delta V_g = 3.84$ V, we obtain $n_0 \approx 2.7 \times 10^{12}$ cm^{-2} to 3.6×10^{12} cm^{-2}, corresponding to a twist angle of ~1.6–2.4° off 0° alignment. Both are consistent with the SHG results.

Determination of the filling fractions. For both the electron and hole sides, the positions of the $|n| = 1/3$, 2/3 and 1 states are identified first. By assuming a linear relation between gate voltage and carrier density, the calibration from gate voltage to filling values can be completely determined by fitting these three data points with a linear line on the respective doping side. Then, for each observed feature, its filling value in decimal format is calculated based on the calibration and then converted to the closest simple fractional format.

Device D2 shows considerable hysteresis (Extended Data Fig. 9). We assume that, at high gate voltages ($|V_g| > 2$ V), the charge density has a linear relation with the gate voltage. We thus only use $|n| = 2/3$ and 1 states for calibration. To justify this approach, we calculated the expected position for the 1/3 filling, which aligns well with the observed 1/3 state. Note that the 1/3 state shows a plateau instead of a sharp minimum because it has a very high resistivity and the MIM signal is therefore saturated at the lower limit (see the MIM response curve in Fig. 1b). If we use the centre of the plateau to identify the actual position for the 1/3 state, the deviation between the centre and the calculated 1/3 position is only $\delta n = 0.023$. For other fine features, we calibrate the filling values based on the gate voltage of the observed minima and assign a closest simple fractional value. For most states, the deviation is <0.0050. The few states with larger deviations ($\delta n < 0.020$) are ±5/6, 5/9 and 3/4. Their best alternative fractional values are 9/11, 6/11 and 16/21, respectively. To check how the ordering pattern changes, we performed simulations for these alternative filling fractions and found that the alternative patterns can be considered as the domain states of the original patterns. The formation of domain boundaries allows the lattice to accommodate extra or missing charges, so that the ordered pattern can be stabilized over a finite range of density around the nominal fractional value. Similar behaviour has been demonstrated in a previous study on charge ordering in a square lattice[39]. In the experiment, this behaviour will lead to a broadening of the dips in the MIM signal. In our data, the simpler fractions fall well within the dips and only have small deviations from the local minima, so we assign the simpler fractions to these features.

MC simulations. The Coulomb lattice gas model was simulated with the Markov chain MC method. Parallel tempering[40] was used to avoid critical slowing down around the transition temperature, and Ewald summation[41] was used to capture the long-range interaction of the Coulomb potential. Most of the simulations were performed in a 12×12 lattice, except for filling fraction 1/7, which was performed on a 14×14 lattice. A 48×48 lattice was also used to examine the formation of domains (Extended Data Figs. 4 and 5). Seventy-two replicas were used and 10 million sweeps were performed for each replica. The temperature list for the replicas was a geometric series starting from $k_B T_1 = 0.01$ with $T_{n+1}/T_n = 1.032$, with $k_B T$ normalized with respect to the Coulomb interaction between NN sites. In each sweep, a simple Metropolis update was used and exchanges between neighbouring replicas were attempted every 10 sweeps. The second half of the sweeps were used to calculate the specific heat C_v. The transition temperatures were estimated from the C_v–T curve (Extended Data Fig. 6) together with the Fourier spectrum of the charge pattern (an example is provided in Extended Data Fig. 7).

Data availability

Data that support the plots within this paper and other findings of this study are available from the corresponding author upon reasonable request. Source data are provided with this paper.

Code availability

The source code for the Monte Carlo simulations is available from the corresponding author upon reasonable request.

References

38. Li, Z. et al. Revealing the biexciton and trion–exciton complexes in BN encapsulated WSe_2. *Nat. Commun.* **9**, 3719 (2018).
39. Rademaker, L., Pramudya, Y., Zaanen, J. & Dobrosavljević, V. Influence of long-range interactions on charge ordering phenomena on a square lattice. *Phys. Rev. E* **88**, 032121 (2013).
40. Swendsen, R. H. & Wang, J.-S. Replica Monte Carlo simulation of spin-glasses. *Phys. Rev. Lett.* **57**, 2607–2609 (1986).
41. Toukmaji, A. Y. & Board, J. A. Ewald summation techniques in perspective: a survey. *Comput. Phys. Commun.* **95**, 73–92 (1996).

Acknowledgements

We thank D. Chen, L. Yan, L. Ma and K. Li for help with device fabrication. We are grateful to R. Swendsen and M. Widom for their help with the Monte Carlo simulation. C.W. and D.X. thank W. Duan for providing part of the computational resources. X.H. and Y.-T.C. acknowledge support from the NSF under award no. DMR-2004701, a Hellman Fellowship award and a seed fund from SHINES, an EFRC funded by the US Department of Energy (DOE), Basic Energy Sciences (BES) under award no. SC0012670. S.M., Z. Li and S.-F.S. acknowledge support by AFOSR through grant no. FA9550-18-1-0312. T.W. and S.-F.S. acknowledge support from ACS PRF through grant no. 59957-DNI10. Z. Lian and S.-F.S. acknowledge support from NYSTAR through Focus Center-NY–RPI contract C150117. Device fabrication was supported by the Micro and Nanofabrication Clean Room (MNCR) at Rensselaer Polytechnic Institute (RPI). S.-F.S. also acknowledges support from the NSF through Career grant no. DMR-1945420. The research by S.O. is supported by the US Department of Energy, Office of Science, Basic Energy Sciences, Materials Sciences and Engineering Division. C.W. and D.X. acknowledge support from DOE, BES grant no. DE-SC0012509. K.W. and T.T. acknowledge support from the Elemental Strategy Initiative conducted by the MEXT (Japan; grant no. JPMXP0112101001), JSPS (KAKENHI grant no. JP20H00354) and the CREST (JPMJCR15F3), JST. We acknowledge computing time provided by BRIDGES at the Pittsburgh Supercomputing Center (award no. TG-DMR190080) under the Extreme Science and Engineering Discovery Environment (XSEDE) supported by the NSF (ACI-1548562).

Author contributions

S.-F.S. and Y.-T.C. initiated the research. T.W., S.M., Z. Li and Z. Lian fabricated the heterostructure devices. X.H. performed the MIM measurements. Y.-T.C., S.-F.S., D.X., S.M., T.W., C.W. and X.H. analysed the data. C.W., S.O. and D.X. performed numerical simulations. Y.-T.C., S.-F.S. and D.X. wrote the manuscript with input from all authors.

Competing interests

The authors declare no competing interests.

Additional information

Extended data is available for this paper at https://doi.org/10.1038/s41567-021-01171-w.

Supplementary Information The online version contains supplementary material available at https://doi.org/10.1038/s41567-021-01171-w.

Correspondence and requests for materials should be addressed to D.X., S.-F.S. or Y.-T.C.

Peer review information *Nature Physics* thanks Fengcheng Wu and the other, anonymous, reviewer(s) for their contribution to the peer review of this work.

Reprints and permissions information is available at www.nature.com/reprints.

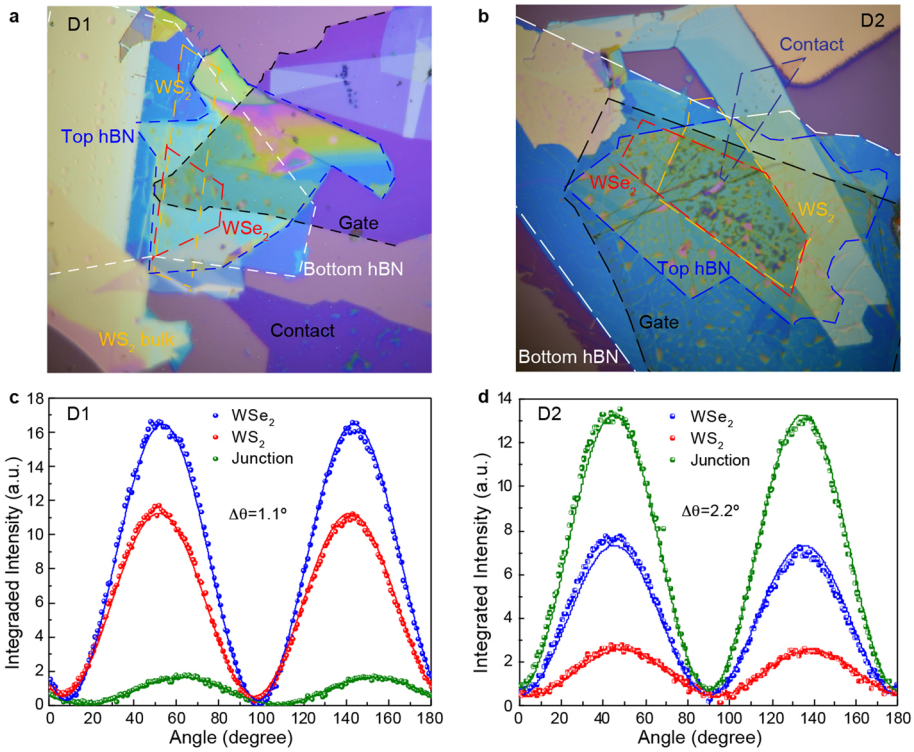

Extended Data Fig. 1 | Sample information. a,b Optical microscope images of devices (**a**) D1 and (**b**) D2 with different flakes outlined. **c,d** Angular dependence of the SHG signal in (**c**) device D1 and (**d**) device D2.

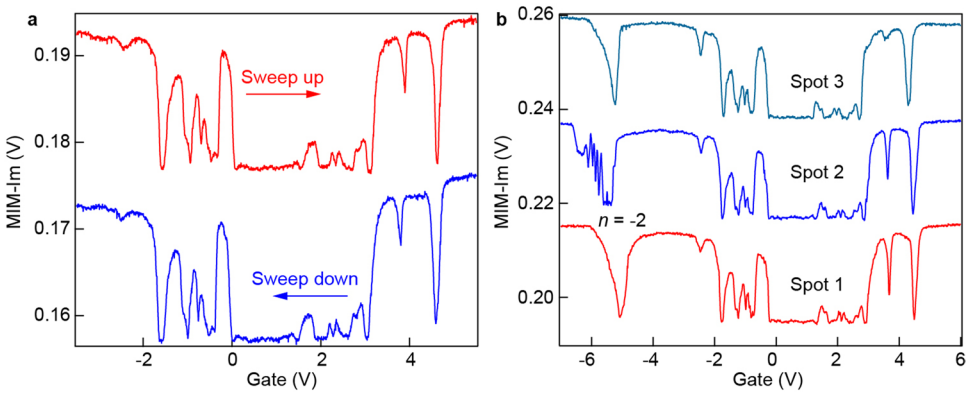

Extended Data Fig. 2 | Additional MIM data in device D1. a, MIM-Im vs gate voltage traces for both sweeping directions in device D1 at $T = 4$ K. **b**, MIM-Im vs gate voltage traces with extended gate range from −7 V to 6 V taken at $T = 3$ K. The feature near −5 V likely correponds to $n = -2$ state. However, due to poor electrical contact at high hole doping, this feature is not stable and its gate position is not repeatable at different spots.

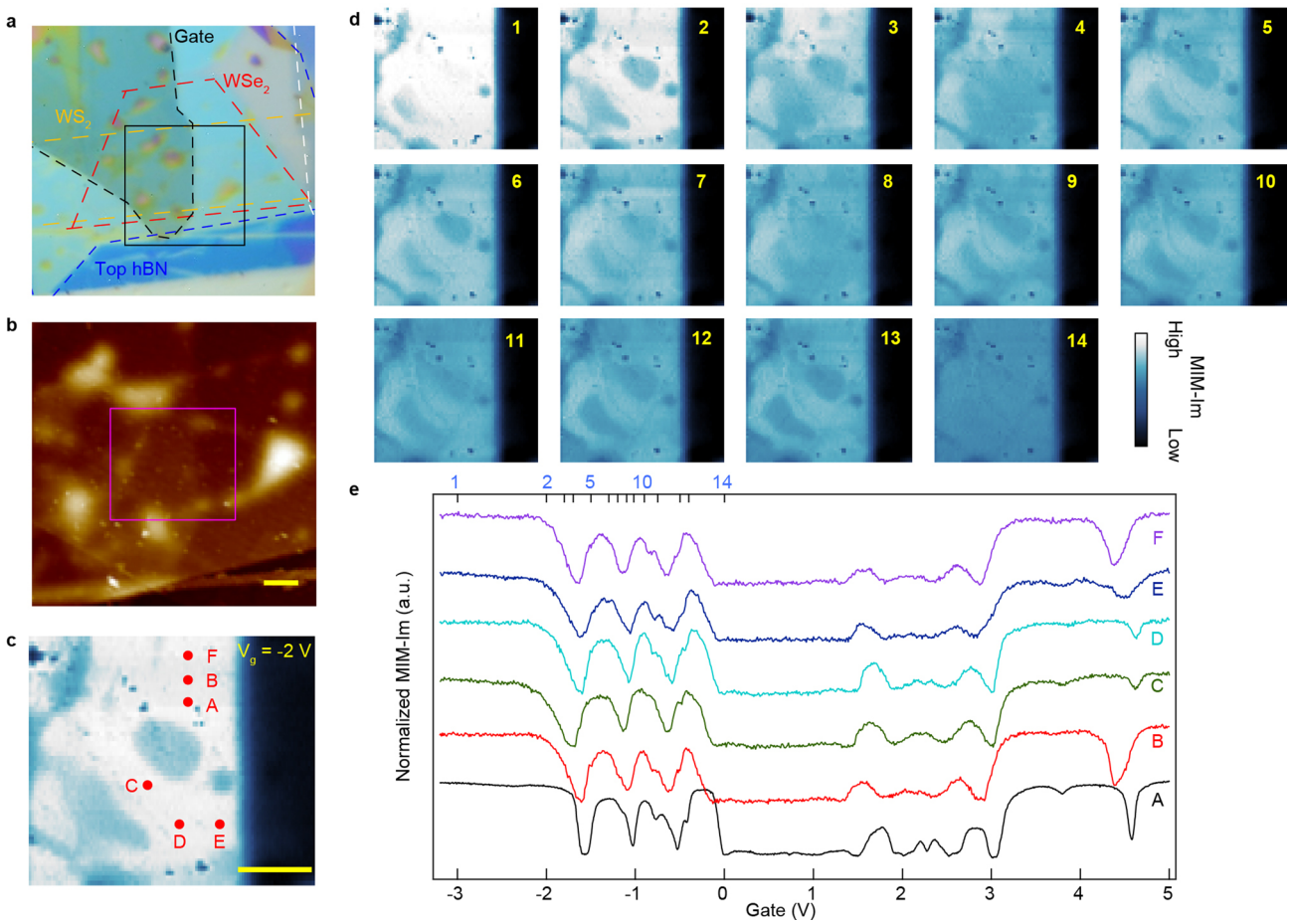

Extended Data Fig. 3 | Spatial uniformity of sample conductivity in device D1. a,b Optical image and atomic force microscopy (AFM) image of device D1. **c**, MIM-Im image at $V_g = -2$ V scanned over the region marked by the rectangles in (**a**) and (**b**). **d**, MIM-Im images taken at different gate voltages marked along the top axis in (**e**). **e**, MIM-Im vs gate traces taken at spots A-F as indicated in (**c**). All MIM data are taken at $T = 10$ K. Scale bars are 2 μm.

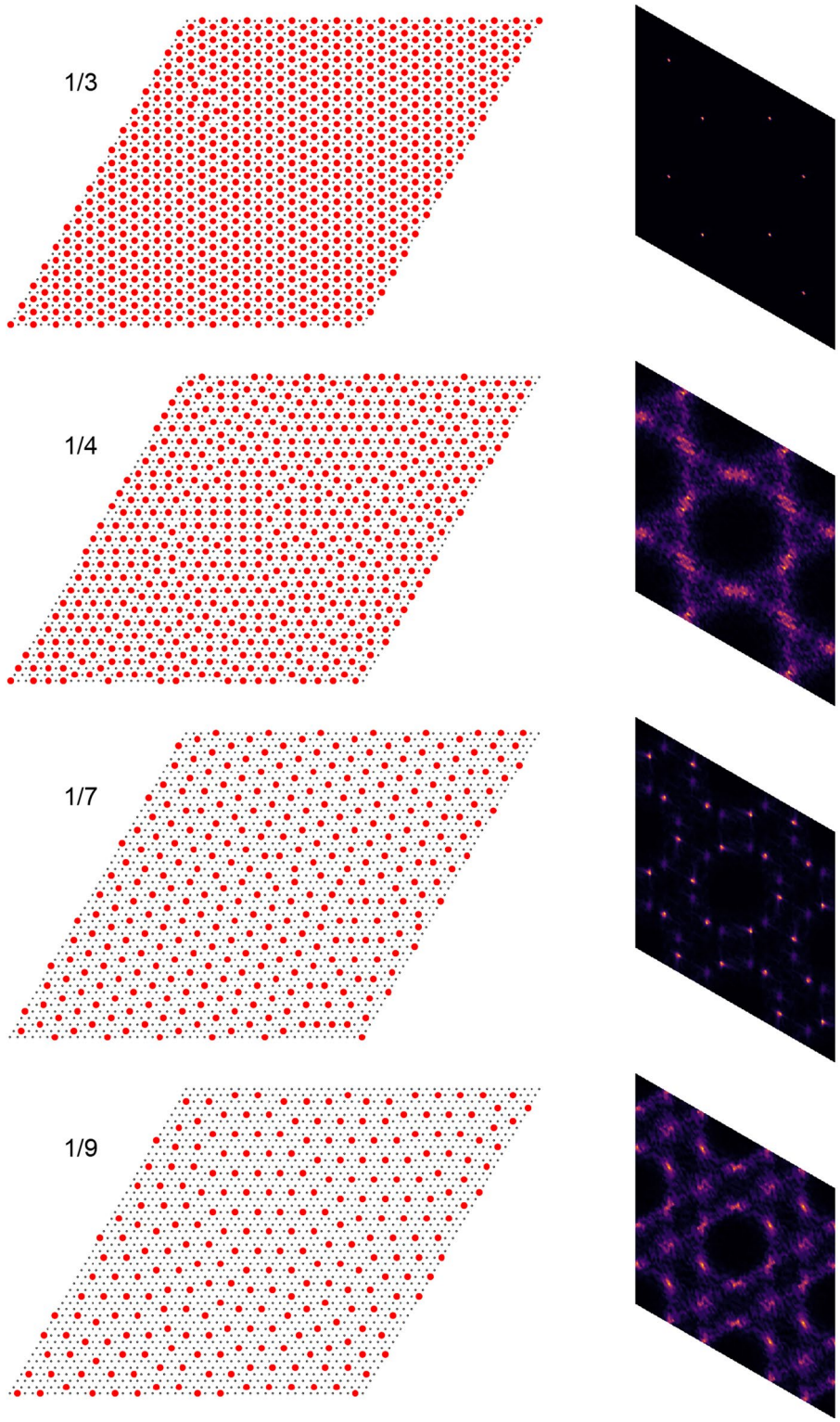

Extended Data Fig. 4 | Ordering patterns simulated on a 48 by 48 lattice for $n = 1/3, 1/4, 1/7,$ and $1/9$. The column on the right plots the fast Fourier transform (FFT) image of the ordering pattern.

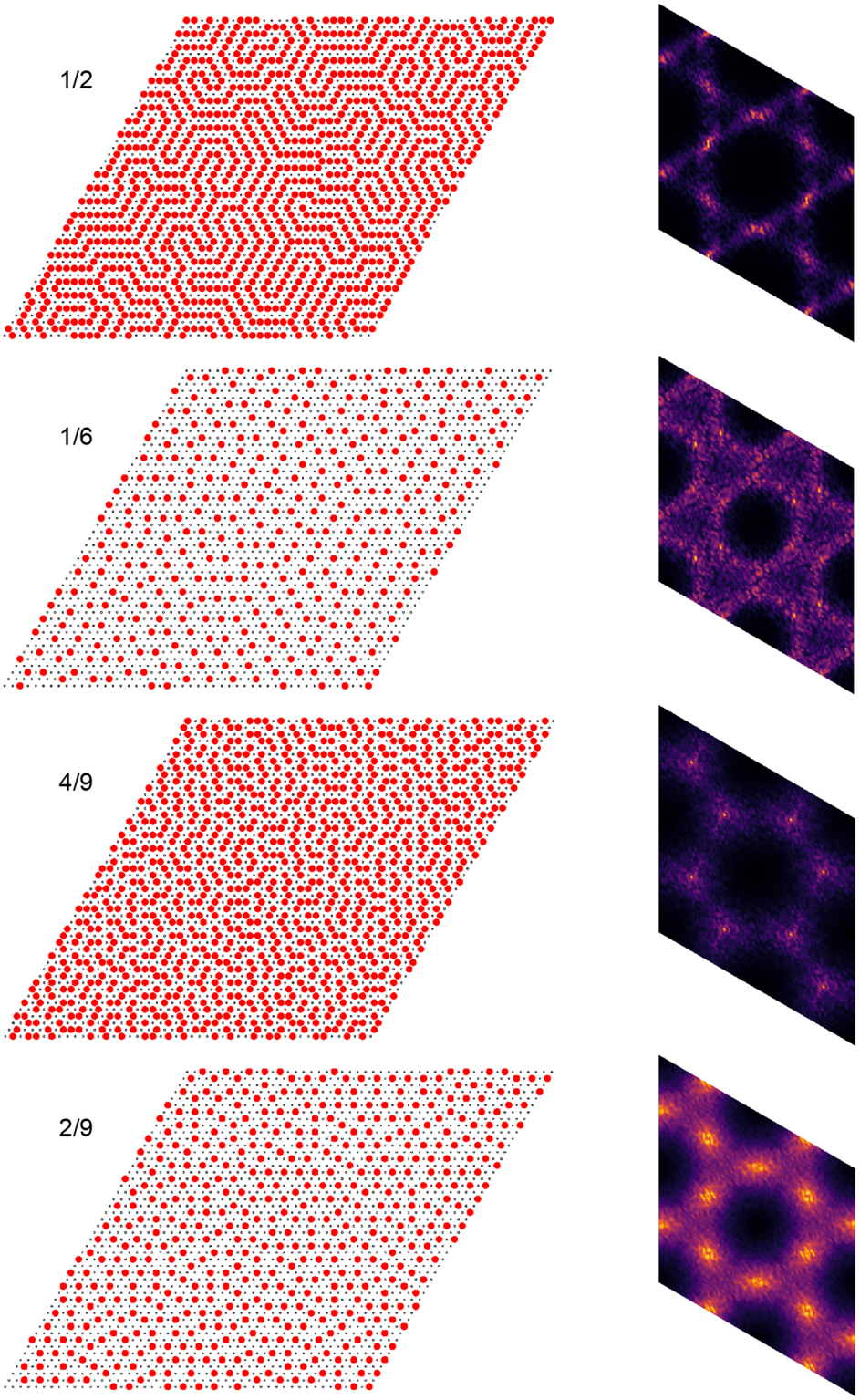

Extended Data Fig. 5 | Ordering patterns simulated on a 48 by 48 lattice for $n = 1/2, 1/6, 4/9,$ and $2/9$. The column on the right plots the FFT image of the ordering pattern.

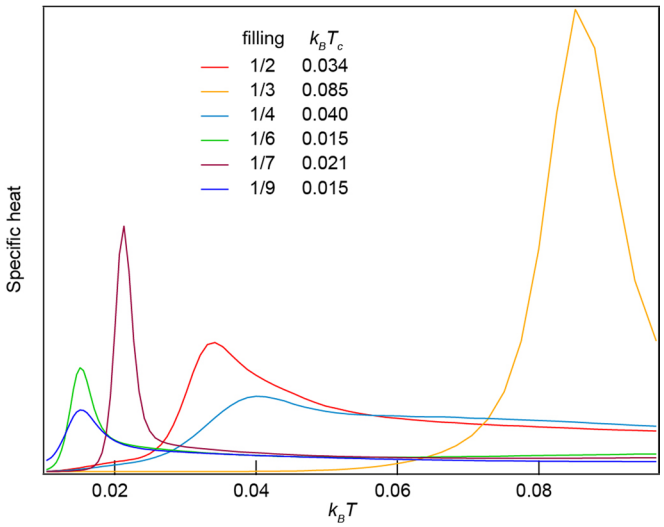

Extended Data Fig. 6 | Simulated specific heat for different fillings. The temperature scale, k_BT, is normalized by the nearest neighbor Coulomb interaction. The identified ordering temperatures, k_BT_c, are listed in the figure.

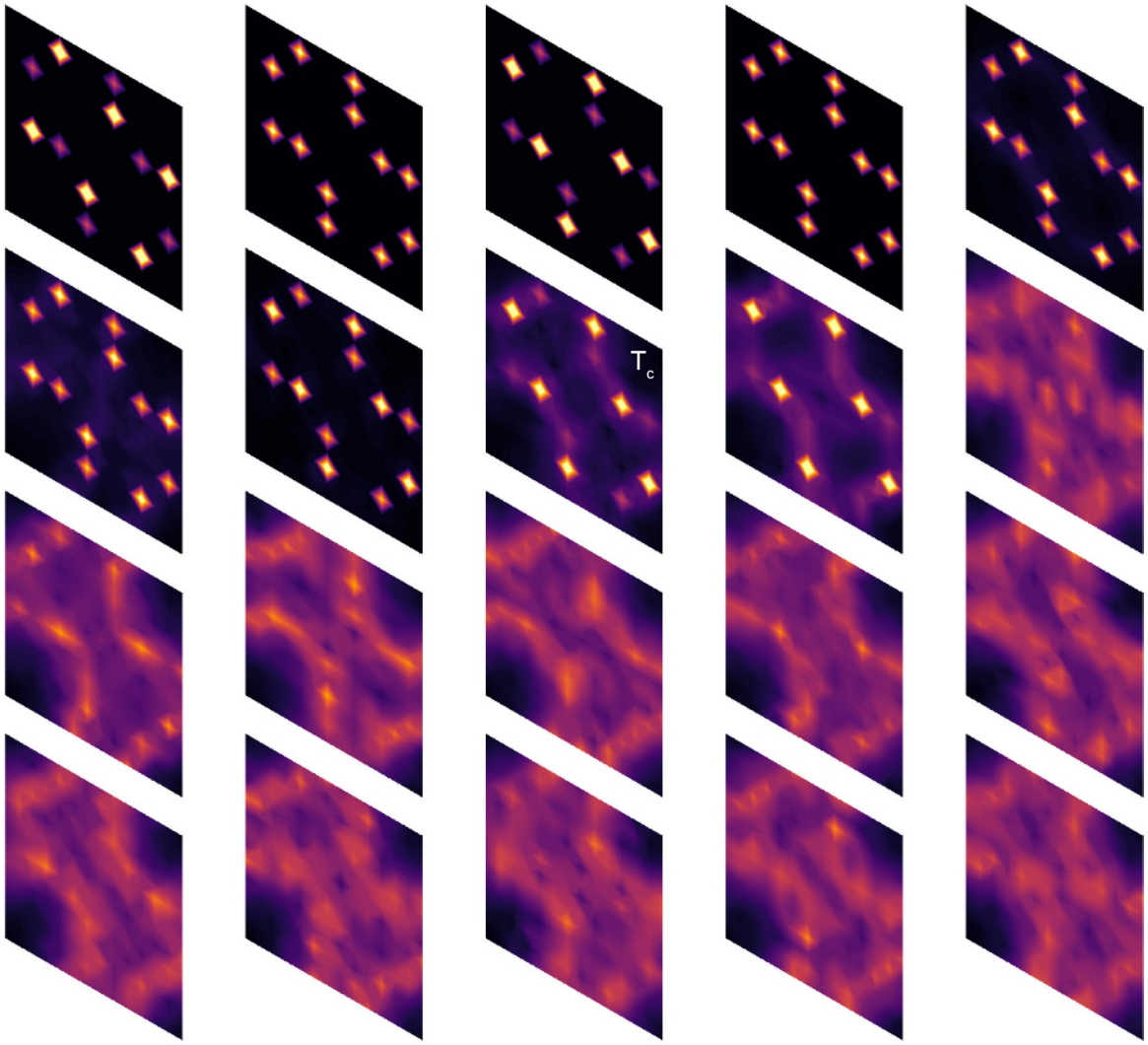

Extended Data Fig. 7 | The Fourier transformed configurations in the reciprocal space as k_BT varies for filling 1/7. The lowest k_BT is 0.017; the highest k_BT is 0.031; $k_BT_c = 0.021$ is labeled in the picture. To visualize the transition around the critical temperature, we select eight configurations from the simulations of 1/7 filling, on which we perform Fourier transformations. The absolute values of the eight Fourier amplitudes are added and plotted in the reciprocal space. It is clear the Fourier amplitudes changes abruptly around T_c, which justifies our approach of identifying the peak in the specific heat as the transition temperature.

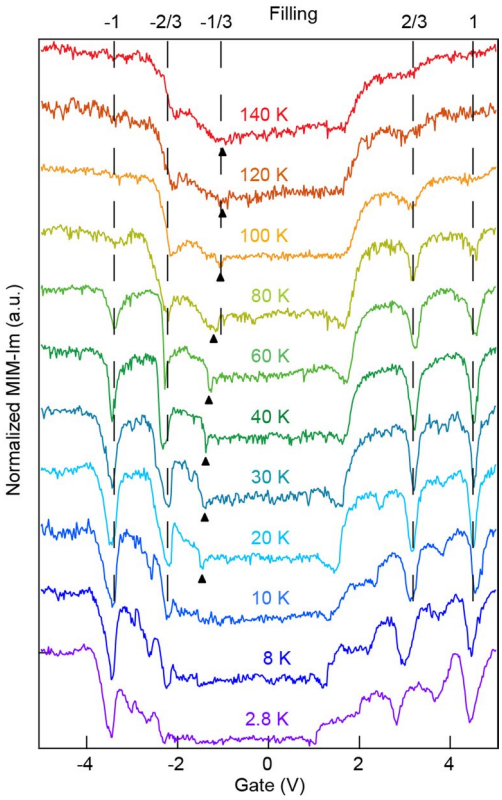

Extended Data Fig. 8 | Temperature dependence of MIM-Im for gate sweeping down from 5 V to -5 V in device D2. The black markers indicate the positions of the $n = -1/3$ state, which can be resolved at temperatures of 20 K and above.

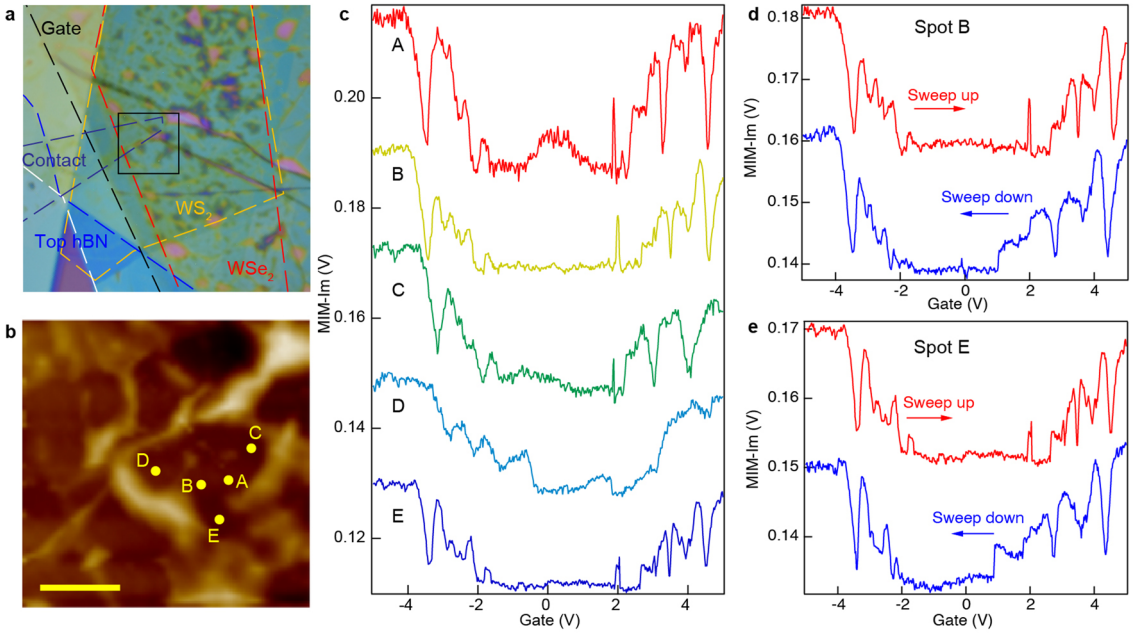

Extended Data Fig. 9 | Spatial variation and hysteresis of the MIM-Im spectrum in device D2. a, Optical microscope of D2. **b**, AFM scan around the area indicated by the solid square in (**a**). The scale bar is 5 μm. **c**, MIM spectra taken at spots A-E as marked in (**b**). **d**, Sweep up and down traces at spot B. **e**, Sweep up and down traces at spot E. All data taken at $T = 2.8$ K.